

Chirality Josephson current due to a novel quantum anomaly in inversion-asymmetric Weyl semimetals

Song-Bo Zhang,¹ Johanna Erdmenger,¹ and Björn Trauzettel¹

¹*Institute for Theoretical Physics and Astrophysics,
University of Würzburg, D-97074 Würzburg, Germany*

(Dated: December 4, 2018)

We study Josephson junctions based on inversion-asymmetric but time-reversal symmetric Weyl semimetals under the influence of Zeeman fields. We find that, due to distinct spin textures, the Weyl nodes of opposite chirality respond differently to an external magnetic field. Remarkably, a Zeeman field perpendicular to the junction direction results in a phase shift of opposite sign in the current-phase relations of opposite chirality. This leads to a finite chirality Josephson current (CJC) even in the absence of a phase difference across the junction. This feature could allow for applications in chiralitytronics. In the long junction and zero temperature limit, the CJC embodies a novel quantum anomaly of Goldstone bosons at π phase difference which is associated with a \mathbb{Z}_2 symmetry at low energies. It can be detected experimentally via an anomalous Fraunhofer pattern.

Introduction.—Weyl semimetals (WSMs) have recently attracted intensive interest thanks to their realization in a number of materials [1–16] and to their novel physics associated with Weyl nodes [17–33]. The Weyl nodes appear in pairs that carry opposite chirality [34] in the absence of time-reversal or inversion symmetry. Chirality is thus a defining emergent property of electrons in WSMs. The possibility to probe and manipulate chirality is one of the most intriguing aspects of WSMs. Recently, chirality-dependent physics has been discussed in various contexts [35–37].

Josephson junctions provide a complementary method to probe the electronic properties of a particular material. They are the basic building blocks for superconducting electronics with applications ranging from electronic magnetometers to quantum computation [38–41]. Hence, it is of fundamental interest to study Josephson junctions based on WSMs. To date, most experimentally relevant WSMs preserve time-reversal symmetry but break inversion symmetry [5–16]. In these materials, s-wave superconductivity couples electrons of the same chirality [42, 43]. Thus, chirality remains a well-defined property in those Josephson junctions. Hence, we could think about using chirality as a resource for electronics, just as spin in spintronics. We coin this idea chiralitytronics. Recently, Josephson junctions based on Dirac semimetals have been fabricated [44–46]. By similar methods, it is feasible to also investigate Josephson junctions based on WSMs. Previous theoretical work [47–51] instead focused on either the inversion-symmetric case or the surface states where chirality is no longer a good quantum number [42, 52].

In this Letter, we focus on Josephson junctions to study the interplay of Zeeman fields, s-wave superconductivity, and chirality in inversion-asymmetric WSMs. We find that the Weyl nodes of opposite chirality display distinct spin textures. Thus, they respond differently to an external magnetic field. As a result, a Zeeman field perpendicular to the junction direction shifts the phase in

the current-phase relations (CPRs) of opposite chirality differently. For each chirality, a Josephson ϕ_0 -junction with a phase shift of opposite sign for opposite chirality is realized. The phase shift is controllable by the junction length and external Zeeman field. The relations between the CPRs can be understood by the underlying low-energy symmetries of the system. Remarkably, this mechanism gives rise to the phenomenon of a finite CJC $J_s^{\text{chi}} \equiv J_s^+ - J_s^-$ with J_s^\pm the Josephson current for each chirality. In the long junction and zero temperature limit, we show that this phenomenon expresses a novel quantum anomaly of Goldstone bosons (Cooper pairs) at π phase difference, since when sending the Zeeman field to zero, the CJC retains a sign singularity, breaking the \mathbb{Z}_2 symmetry between the two decoupled chirality sectors at the quantum level. This mechanism also manifests itself as an anomalous Fraunhofer pattern.

Model and setup.—We consider inversion-asymmetric WSMs described by the Hamiltonian [43, 53] $\mathcal{H}_w = \sum_{\mathbf{k}} \psi_{\mathbf{k}}^\dagger H(\mathbf{k}) \psi_{\mathbf{k}}$ with

$$H(\mathbf{k}) = k_x \sigma_x s_z + k_y \sigma_y s_0 + (\kappa_0^2 - |\mathbf{k}|^2) \sigma_z s_0 + \beta \sigma_y s_y - \alpha k_y \sigma_x s_y, \quad (1)$$

where $\psi_{\mathbf{k}}^\dagger = (c_{A,\uparrow,\mathbf{k}}^\dagger, c_{A,\downarrow,\mathbf{k}}^\dagger, c_{B,\uparrow,\mathbf{k}}^\dagger, c_{B,\downarrow,\mathbf{k}}^\dagger)$, $c_{\sigma,s,\mathbf{k}}^\dagger$ are creation operators with orbital indices $\sigma = A, B$, spin indices $s = \uparrow, \downarrow$, and wave vector \mathbf{k} ; σ_i ($i = x, y, z, 0$) are Pauli and 2×2 unit matrices for orbital space, and s_i for spin space. κ_0 , α and β are real model parameters. Suppose $0 < \beta < \kappa_0$, there are four Weyl nodes at $\mathbf{Q}_{1,2} = \pm(\beta, 0, k_0)$ and $\mathbf{Q}_{3,4} = \pm(\beta, 0, -k_0)$, respectively, where $k_0 = (\kappa_0^2 - \beta^2)^{1/2}$. At low energies, the model (1) can be approximated as a sum of four Weyl Hamiltonians, $\mathcal{H}_w = \sum_{\gamma=1}^4 \sum_{\mathbf{k}} \Psi_{\gamma,\mathbf{k}}^\dagger H_\gamma(\mathbf{k}) \Psi_{\gamma,\mathbf{k}}$ with

$$\begin{aligned} H_{1(2)}(\mathbf{k}) &= (k_x \mp \beta) s_x + k_y s_y + (k_z \mp k_0) s_z, \\ H_{3(4)}(\mathbf{k}) &= (k_x \mp \beta) s_x + k_y s_y - (k_z \pm k_0) s_z, \end{aligned} \quad (2)$$

where k_y has been rescaled by $1/\alpha$ and k_z by $1/(2k_0)$ [43]. $\gamma (= 1, 2, 3, 4)$ labels the Weyl node at \mathbf{Q}_γ . Accordingly,

Weyl nodes 1 and 2 carry positive chirality, while Weyl nodes 3 and 4 carry negative chirality. $\sum_{\mathbf{k}}$ means that \mathbf{k} is confined in the sum to the vicinity of Weyl nodes. The spinors $\Psi_{\gamma,\mathbf{k}} \equiv (\psi_{\gamma,\uparrow,\mathbf{k}}, \psi_{\gamma,\downarrow,\mathbf{k}})^\dagger$ of Weyl nodes are given by $\Psi_{1,\mathbf{k}} = \Psi_{3,\mathbf{k}} = (c_{\uparrow,\mathbf{k}}^{(B)\dagger}, c_{\downarrow,\mathbf{k}}^{(A)\dagger})$ and $\Psi_{2,\mathbf{k}} = \Psi_{4,\mathbf{k}} = (c_{\uparrow,\mathbf{k}}^{(A)\dagger}, c_{\downarrow,\mathbf{k}}^{(B)\dagger})$ with $c_{\uparrow(\downarrow),\mathbf{k}}^{(\sigma)} = (c_{\sigma,\uparrow,\mathbf{k}} \pm c_{\sigma,\downarrow,\mathbf{k}})/\sqrt{2}$. While the indices $s = \uparrow, \downarrow$ in the operators $c_{\sigma,s,\mathbf{k}}$ denote spin-up and spin-down in z direction, respectively, $s' = \uparrow, \downarrow$ in the new basis $\psi_{\gamma,s',\mathbf{k}} = c_{s',\mathbf{k}}^{(\sigma)}$ denote spin-up and spin-down in x direction, respectively. We can readily observe that Weyl nodes of opposite chirality display distinct spin textures or spin-momentum locking as shown in Fig. 1(a).

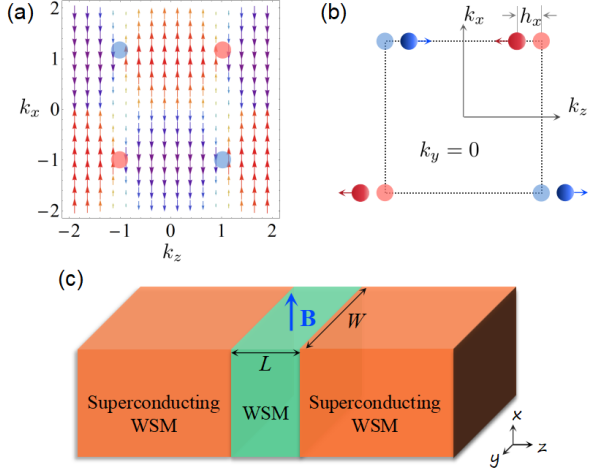


Figure 1. (a) Spin texture of the lower conduction band of the model (1) at $k_y = 0$ with $\kappa_0 = \sqrt{2}$ and $\beta = 1$; (b) Position shifts of Weyl nodes in momentum space due to the Zeeman field h_x in x direction. The red (blue) dots denote the Weyl nodes of positive (negative) chirality; (c) Sketch of the Weyl Josephson junction.

The distinct spin textures near Weyl nodes of opposite chirality imply different responses of Weyl nodes to Zeeman fields. A Zeeman field $\mathbf{h} = g\mu_B\mathbf{B}/2 \equiv (h_x, h_y, h_z)$ couples to the electron spin via $H_Z = \sigma_0\mathbf{h}\cdot\mathbf{s}$ in our model (1), where g is the g-factor, μ_B the Bohr magneton and \mathbf{B} the magnetic field. The y - and z -components h_y and h_z couple electrons from different Weyl nodes, whereas the x -component h_x couples electrons not only from different Weyl nodes but also acts within each Weyl node. Therefore, after projecting \mathbf{h} to low energies, only h_x is significant [54, 63]. It gives rise to a diagonal term

$$H_\gamma^Z = h_x s_z \quad (3)$$

for each Weyl node. Combining Eq. (3) with Eq. (2), it is interesting to see that the positions of the Weyl nodes of positive (negative) chirality are shifted oppositely by $\mp h_x$ in k_z direction, as depicted in Fig. 1(b). Thus, h_x can be viewed as a constant axial-vector potential $A_z^a = \hbar h_x/e$ in z direction which acts with opposite sign on Weyl nodes of opposite chirality.

Next, we introduce s-wave superconducting pairing with both intra- and interorbital components to this problem. As shown in Ref. [43], at low energies only the intraorbital pairing is important and it couples Weyl nodes of the same chirality. Thus, the full system can be considered at low energies as two effectively decoupled sectors with opposite chirality, respectively.

Finally, we consider a Josephson junction formed by sandwiching a WSM between two s-wave superconducting WSMs, as sketched in Fig. 1(c). The positive chirality sector can then be described by the Bogoliubov-de Gennes (BdG) Hamiltonian [64]

$$h_{\text{BdG}}^+ = \nu_z \tau_0 [-i\partial_{\mathbf{r}} \cdot \mathbf{s} - \mu(\mathbf{r})s_0] + h(\mathbf{r})\nu_0 \tau_0 s_z + \Delta_s(\mathbf{r})e^{i\text{sgn}(z)\phi\nu_z/2}\nu_x \tau_x s_0 \quad (4)$$

in the Nambu basis $(\psi_{1,\uparrow}, \psi_{1,\downarrow}, \psi_{2,\downarrow}, -\psi_{2,\uparrow}, \psi_{2,\uparrow}, \psi_{2,\downarrow}, \psi_{1,\downarrow}, -\psi_{1,\uparrow})$, $\Delta_s(\mathbf{r}) = \Delta\Theta(|z| - L/2)$ is the pairing potential, ϕ the phase difference across the junction and L the junction length; $\Theta(z)$ is the Heaviside function and $\text{sgn}(z)$ the sign function. The Zeeman field is applied to the normal WSM in x direction, $h(\mathbf{r}) = h_x\Theta(L/2 - |z|)$; $\mu(\mathbf{r}) = \mu_S\Theta(|z| - L/2) + \mu_N\Theta(L/2 - |z|)$ is the chemical potential. The Pauli and 2×2 unit matrices τ_i and ν_i ($i=x, y, z, 0$) act on Weyl-node and particle-hole spaces, respectively. The BdG Hamiltonian h_{BdG}^- for the negative chirality sector can be obtained by replacing ∂_z by $-\partial_z$ in Eq. (4).

Josephson current of one chirality sector.—In order to determine the Josephson current, we adapt the method of Refs. [65–67] which takes into account both contributions from Andreev bound states and the continuum spectrum. Throughout the Letter, we normalize the current densities by the corresponding normal-state resistance R_n of the junction at zero temperature [54].

First, let us analyze the case without Zeeman fields. There, we find that the Josephson currents of the two chiralities are identical, reflecting a \mathbb{Z}_2 symmetry of the system at low energies which we further discuss below. The results for positive chirality at low temperature are shown in Fig. 2. The Josephson current is 2π -periodic in the phase difference ϕ . It vanishes at $\phi = 0$ and $\pm\pi$ as required by time-reversal symmetry. The critical current density $J_c^+ \equiv \max[J_s^+(\phi)]$ decays on increasing L . At $\mu_N \approx \mu_S$, $J_c^+ R_n$ is maximized [Fig. 2(c)], indicating the enhancement of Andreev reflection at the N-S interfaces [43]. Interestingly, we predict a clear forward skewness in the CPRs at low temperatures $k_B T \ll \min\{\Delta, 1/L\}$. This skewness is related to the helical nature of Andreev bound states [68, 69] due to strong spin-momentum locking in WSMs. At $\mu_N \approx \mu_S$, a more pronounced skewness can be observed [Fig. 2(d)].

The most exciting physics arises in the presence of the Zeeman field h_x . We find that h_x shifts the phase difference ϕ by $\phi_0 = 2h_x L$ as it enters as an effective vector potential in z direction. Consequently, J_s^+ becomes zero

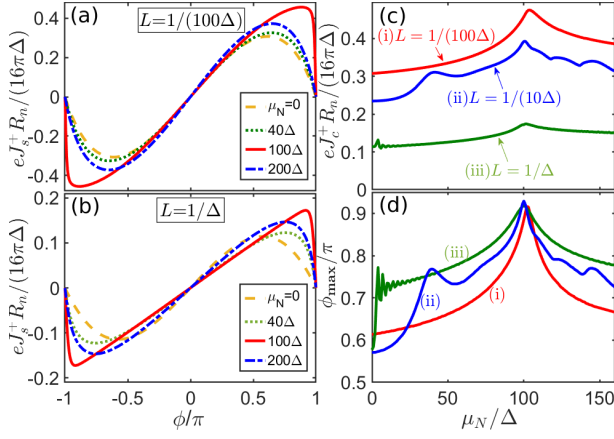


Figure 2. Current-phase relations for positive chirality in the absence of Zeeman fields for $L = 1/(100\Delta)$ (a) and $1/\Delta$ (b) with various choices of μ_N ; (c) Critical current density J_c^+ as a function of μ_N for $L = 1/(100\Delta)$ (i, red), $1/(10\Delta)$ (ii, blue), and $1/\Delta$ (iii, green), respectively; (d) Location ϕ_{\max} of J_c^+ , a measurement of skewness, as a function of μ_N for (i), (ii), and (iii), respectively. $\mu_S = 100\Delta$ and $k_B T = 0.01\Delta$ in all plots.

neither at $\phi = 0$ nor $\pm\pi$. An anomalous Josephson current $J_s^+(\phi = 0) \neq 0$ can be obtained, due to the presence of the phase shift ϕ_0 (green curves in Fig. 3). The system indeed realizes a Josephson ϕ_0 -junction [70] for positive chirality with the phase shift tunable by the Zeeman field and junction length. Importantly, similar results can be found for negative chirality but with a phase modulation of opposite sign $-\phi_0$ (yellow curves in Fig. 3). Therefore, the supercurrents of opposite chirality become different, i.e., $J_s^-(\phi) \neq J_s^+(\phi)$. This implies the striking phenomenon of a finite CJC. Note that supercurrents of opposite chirality can still be related to each other by $J_s^-(\phi) = -J_s^+(-\phi)$, as a result of a magnetic \mathbb{Z}_2 symmetry between the two chirality sectors [54].

Total and chirality Josephson currents.—With the obtained $J_s^\pm(\phi)$, we are equipped to evaluate the total and chirality Josephson currents. The results for the total Josephson current $J_s^{\text{tot}}(\phi) \equiv J_s^+(\phi) + J_s^-(\phi)$ are represented by the blue curves in Fig. 3. In the absence of ϕ_0 , the CPRs for each chirality are identical. Thus, $J_s^{\text{tot}}(\phi)$ takes exactly the same form as $J_s^+(\phi)$ but twice as large. In contrast, the presence of ϕ_0 shifts the CPRs of opposite chirality oppositely, which, along with the forwardly skewed shape of $J_s^\pm(\phi)$, leads to several particular features in $J_s^{\text{tot}}(\phi)$. First, the contributions of the two chiralities to $J_s^{\text{tot}}(\phi)$ is controllable by ϕ_0 . At $\phi = \pm\phi_0 + n\pi$, $n \in \mathbb{Z} \equiv \{0, \pm 1, \dots\}$, $J_s^{\text{tot}}(\phi)$ is of purely positive (negative) chirality. This feature can be exploited in superconducting chiralitytronics, since we are able to transfer a net chirality across the junction via dissipationless transport of chiral Cooper pairs. Second, with increasing ϕ_0 from 0 to $\pi/2$, the maximum of $J_s^{\text{tot}}(\phi)$ decreases

monotonically but never goes to zero [inset in Fig. 3(d)]. Meanwhile, the slope of $J_s^{\text{tot}}(\phi)$ at $\phi = (2n+1)\pi$, $n \in \mathbb{Z}$, changes its sign at a critical ϕ_0 . Then, two instead of one peak (dip) appear in a period $\phi \in [-\pi, \pi]$ [Fig. 3(b)]. Third, for $\phi_0 = (2n+1)\pi/2$, $n \in \mathbb{Z}$, the two peaks (dips) become equal. Hence, $J_s^{\text{tot}}(\phi)$ becomes π instead of 2π periodic in ϕ and takes a more skewed shape [Fig. 3(c)]. Fourth, for $\phi_0 = n\pi$, $n \in \{\pm 1, \pm 3, \dots\}$, $J_s^{\text{tot}}(\phi)$ resembles the one of a π -junction [Fig. 3(d)]. This means that tuning ϕ_0 leads to a 0 - π transition in $J_s^{\text{tot}}(\phi)$. Finally, although time-reversal symmetry is broken by h_x in the system, $J_s^{\text{tot}}(\phi)$ still obeys $J_s^{\text{tot}}(\phi) = -J_s^{\text{tot}}(-\phi)$. Thus, $J_s^{\text{tot}}(\phi)$ always vanishes at $\phi = n\pi$, $n \in \mathbb{Z}$.

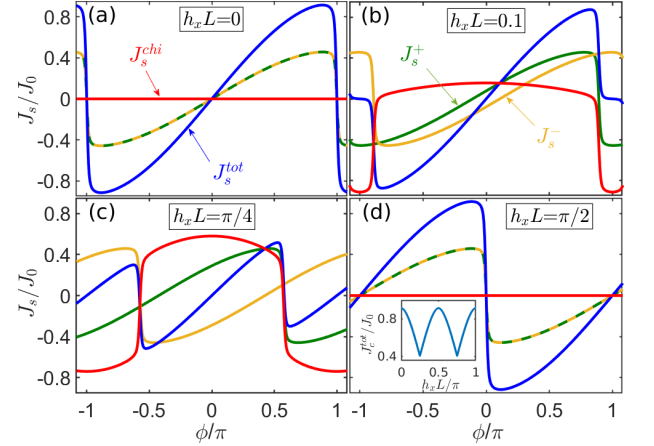


Figure 3. Current-phase relations for $h_x L = 0, 0.1, \pi/4$, and $\pi/2$, respectively. The green, yellow, blue and red curves represent J_s^+ , J_s^- , J_s^{tot} and J_s^{chi} , respectively. The inset in panel (d) illustrates the maximum of J_s^{tot} as a function of $h_x L$. $J_0 = 16\pi\Delta/(eR_n)$, $L = 1/(100\Delta)$, $\mu_N = \mu_S = 100\Delta$ and $k_B T = 0.01\Delta$ in all plots.

The red curves in Fig. 3 show the results for the CJC $J_s^{\text{chi}}(\phi) \equiv J_s^+(\phi) - J_s^-(\phi)$. Without Zeeman fields, i.e., $\phi_0 = 0$, $J_s^{\text{chi}}(\phi)$ is always vanishing, as the supercurrents of opposite chirality $J_s^\pm(\phi)$ are the same [Fig. 3(a)]. In contrast, an applied Zeeman field h_x in the N region leads to chirality-dependent phase shifts $\pm\phi_0$ in the CPRs, making $J_s^\pm(\phi)$ generally different. Thus, a finite CJC $J_s^{\text{chi}}(\phi) \neq 0$ is allowed, as shown in Fig. 3(b, c). Different from the total Josephson current, $J_s^{\text{chi}}(\phi)$ is always 2π -periodic in ϕ . Moreover, $J_s^{\text{chi}}(\phi)$ is an even function of ϕ , i.e., $J_s^{\text{chi}}(\phi) = J_s^{\text{chi}}(-\phi)$. This indicates that a finite J_s^{chi} exists even in the absence of a phase difference. Interestingly, the maxima of $|J_s^{\text{chi}}(\phi)|$ always occur at $\phi = n\pi$, $n \in \mathbb{Z}$ (where $J_s^{\text{tot}} = 0$) and are twice as large as $|J_s^\pm(\phi)|$ there. In the case $\mu_N \approx \mu_S$, salient dips may occur at $\phi = (2n+1)\pi$, $n \in \mathbb{Z}$ for small ϕ_0 , due to the pronouncedly skewed shape of $J_s^\pm(\phi)$. Additionally, the anomalous CJC $J_s^{\text{chi}}(0)$ is an odd and oscillatory function of ϕ_0 with a period of 2π .

Quantum anomaly of Goldstone bosons.—In the Weyl Josephson junction without Zeeman fields, the two chiral-

ity sectors at low energies are connected by a \mathbb{Z}_2 exchange symmetry,

$$\mathcal{U}H_+(\mathbf{r})\mathcal{U}^{-1} = H_-(\mathbf{r}), \quad \mathcal{U} = i\tau_y s_y \mathcal{R}_x, \quad (5)$$

where the basis is $(c_{\uparrow}^{(B)}, c_{\downarrow}^{(A)}, c_{\uparrow}^{(A)}, c_{\downarrow}^{(B)})$, $H_+(\mathbf{r}) = \text{diag}(H_1(\mathbf{r}), H_2(\mathbf{r}))$ and $H_-(\mathbf{r}) = \text{diag}(H_3(\mathbf{r}), H_4(\mathbf{r}))$ the Hamiltonians for Weyl fermions of positive and negative chirality, respectively, $H_\gamma(\mathbf{r})$ the Fourier transforms of $H_\gamma(\mathbf{k})$ in Eq. (2), and \mathcal{R}_x the reflection operator about the yz plane [54]. The two chirality sectors have identical response to a phase difference ϕ across the junction, as superconductivity preserves this \mathbb{Z}_2 symmetry. This leads to $J_s^+(\phi) = J_s^-(\phi)$ for all ϕ . Therefore, $J_s^{\text{chi}}(\phi)$ is vanishing. However, the Zeeman field h_x plays the role of an axial-vector potential in the system. It effectively modifies the phase difference, leading to a finite CJC. This CJC is closely associated with the \mathbb{Z}_2 symmetry, different from the anomalous Josephson effects discussed previously in a variety of 1D systems with broken chiral symmetry [70, 71].

We now carefully explain in which sense the presence of a finite J_s^{chi} corresponds to a quantum anomaly of Goldstone bosons. In the long junction and zero temperature limit, $T = 0$ and $L \gg 1/\Delta$, the contribution to the supercurrent comes from low-energy Andreev bound states with energy $|\epsilon| \ll \Delta$ [72, 73]. For each \mathbf{k}_{\parallel} , the energy levels cross at $\phi \pm \phi_0 = \pi$ for the positive and negative chirality sectors, respectively. Summing over all allowed \mathbf{k}_{\parallel} , the CJC for fixed $\phi = \pi$ shows a discontinuous jump at $h_x = 0$ [54]. Namely,

$$J_s^{\text{chi}} = \frac{2\mu_N^2}{3L} \left[\frac{2h_x L}{\pi} - \text{sgn}(h_x) \right], \quad |h_x L| < \pi. \quad (6)$$

This result is robust against a non-magnetic perturbations such as an interface barrier or smooth disorder in the N region [54]. The amplitude of J_s^{chi} is determined by the density of states of Weyl fermions at the Fermi level in the N region, and it depends quadratically on μ_N . When $h_x \rightarrow 0$, the system is invariant under the \mathbb{Z}_2 exchange. However, J_s^{chi} retains the noninvariant contribution with an ambiguous sign, which contradicts the prediction that $J_s^{\text{chi}} = 0$ in the presence of the \mathbb{Z}_2 symmetry. Therefore, this discontinuity corresponds to a quantum anomaly of Cooper pairs somewhat similar to the mirror anomaly proposed by Burkov [74] but associated with the \mathbb{Z}_2 symmetry of Eq. (5). Note that the quantum anomaly is restricted to a specific parameter regime (i.e., for $\phi = \pi$, $T = 0$ and $L \gg 1/\Delta$).

Anomalous Fraunhofer pattern.—In the Weyl Josephson junction, the magnetic field B_x applied to the N region also modulates the phase difference spatially [75]. The total supercurrent through the junction is then given by

$$I_s = \frac{W\Phi_0}{2\pi\Phi} \int_{-\pi\Phi/\Phi_0+\gamma_0}^{\pi\Phi/\Phi_0+\gamma_0} d\phi J_s^{\text{tot}}(\phi). \quad (7)$$

Here, $J_s^{\text{tot}}(\phi)$ is taking into account the modification by the Zeeman field; γ_0 is the phase difference at $y = 0$; $\Phi = B_x W L$ the magnetic flux threading the N region; W the junction width; Φ_0 the flux quantum. Plotting the maximum supercurrent $I_c = \max[I_s(\gamma_0)]$ as a function of B_x or Φ yields the Fraunhofer pattern [75].

With the previously obtained CPRs plugged into Eq. (7), the Fraunhofer patterns are readily calculated and displayed in Fig. 4. The Fraunhofer pattern strongly depends on the quantity $\tilde{g} \equiv g\mu_B\Phi_0/W$. When \tilde{g} is negligible, $\tilde{g} \ll 1$, such as in a wide junction with a small g -factor, we have a conventional Fraunhofer pattern shape, i.e., $I_c(\Phi)/I_c(0) = (\Phi_0/\Phi)|\sin(\pi\Phi/\Phi_0)|$ [Fig. 4(a)]. For $\tilde{g} \gtrsim 1$, more (local) maxima appear and their values do not decay monotonically with increasing Φ or B_x anymore [Fig. 4(b, c, d)]. For a large $\tilde{g} \gtrsim 10$ such as in a narrow junction with a large g -factor, the Fraunhofer pattern exhibits a beating behavior with two frequencies [Fig. 4(d)]. We note that these anomalous Fraunhofer patterns, originating from the interference of the supercurrents of different chirality, are a manifestation of the chirality-dependent phase shifts in the CPRs due to the Zeeman field.

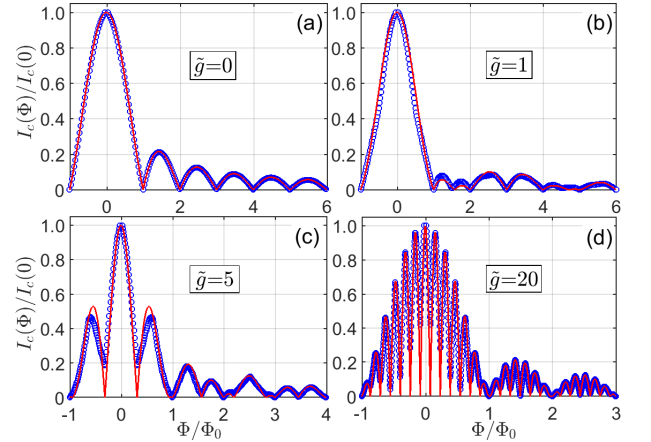


Figure 4. Fraunhofer patterns for $\tilde{g} = 0, 1, 5$, and 20 , respectively. The blue circled curves are calculated from Eq. (7), while the red curves are plots of Eq. (S5.1) in Ref. [54]. $L = 1/(100\Delta)$, $\mu_S = \mu_N = 100\Delta$ and $k_B T = 0.01\Delta$ in all plots.

Discussion and summary.—We briefly discuss the applicability of our results to experiments. In the candidate material of compressively strained HgTe, $g \simeq 22.5$ [76]. Consider a typical Fermi velocity of $v_F \simeq 10^5$ m/s. Then, at a magnetic field $B_x = 10$ mT, the position shift of Weyl nodes is $\delta k_z \simeq 10^{-4} \text{ nm}^{-1}$ which is one or two orders of magnitude smaller than the separation of Weyl nodes [15]. For junctions with lengths larger than 500 nm, we could hence obtain an observable phase shift $\phi_0 \gtrsim 0.1$. In order to have $\tilde{g} \gtrsim 1$, a junction width smaller than 40 nm is needed in this material.

In summary, we find that in Josephson junctions based

inversion-asymmetric WSMs, a perpendicular Zeeman field can realize chirality-dependent ϕ_0 -junctions and gives rise to a finite CJC which occurs even without a phase difference. This can be understood by the distinct spin textures near Weyl nodes of opposite chirality. This effect shows a novel quantum anomaly of Goldstone bosons in a specific parameter regime and manifests itself as an anomalous Fraunhofer pattern.

Acknowledgments.—We would like to thank J. Bardarson, D. Breunig, P. Bureset, A. Cappelli, F. Dominguez, C. Fleckenstein, H. Hansson, M. Stehno, G. Tang, N. Traverso Ziani, S. Upadhyay, and X. Wu for useful discussions. This work was supported by the DFG (SPP1666 and SFB1170 "ToCoTronics") and the ENB Graduate School on "Topological Insulators".

-
- [1] P. Hosur and X. Qi, "Recent developments in transport phenomena in Weyl semimetals," *C. R. Phys.* **14**, 857 (2013).
 - [2] A. M. Turner and A. Vishwanath, "Beyond band insulators: Topology of semi-metals and interacting phases," [arXiv:1301.0330](https://arxiv.org/abs/1301.0330).
 - [3] A. A. Burkov and L. Balents, "Weyl semimetal in a topological insulator multilayer," *Phys. Rev. Lett.* **107**, 127205 (2011).
 - [4] G. B. Halász and L. Balents, "Time-reversal invariant realization of the Weyl semimetal phase," *Phys. Rev. B* **85**, 035103 (2012).
 - [5] M. Hirayama, R. Okugawa, S. Ishibashi, S. Murakami, and T. Miyake, "Weyl node and spin texture in trigonal tellurium and selenium," *Phys. Rev. Lett.* **114**, 206401 (2015).
 - [6] H. M. Weng, C. Fang, Z. Fang, B. A. Bernevig, and X. Dai, "Weyl semimetal phase in noncentrosymmetric transition-metal monophosphides," *Phys. Rev. X* **5**, 011029 (2015).
 - [7] S. M. Huang, S. Y. Xu, I. Belopolski, C. C. Lee, G. Chang, B. K. Wang, N. Alidoust, G. Bian, M. Neupane, C. Zhang, S. Jia, A. Bansil, H. Lin, and M. Z. Hasan, "A Weyl fermion semimetal with surface Fermi arcs in the transition metal monpnictide TaAs class," *Nat. Commun.* **6**, 7373 (2015).
 - [8] T. Rauch, S. Achilles, J. Henk, and I. Mertig, "Spin chirality tuning and topological semimetals in strained $\text{HgTe}_x\text{S}_{1-x}$," *Phys. Rev. Lett.* **114**, 236805 (2015).
 - [9] S. Y. Xu, I. Belopolski, N. Alidoust, M. Neupane, G. Bian, C. L. Zhang, R. Sankar, G. Q. Chang, Z. J. Yuan, C. C. Lee, S. M. Huang, H. Zheng, J. Ma, D. S. Sanchez, B. K. Wang, A. Bansil, F. C. Chou, P. P. Shibayev, H. Lin, S. Jia, and M. Z. Hasan, "Discovery of a Weyl fermion semimetal and topological Fermi arcs," *Science* **349**, 613 (2015).
 - [10] L. X. Yang, Z. K. Liu, Y. Sun, H. Peng, H. F. Yang, T. Zhang, B. Zhou, Y. Zhang, Y. F. Guo, M. Rahn, D. Prabhakaran, Z. Hussain, S.-K. Mo, C. Felser, B. Yan, and Y. L. Chen, "Weyl semimetal phase in the non-centrosymmetric compound TaAs," *Nat Phys* **11**, 728–732 (2015).
 - [11] B. Q. Lv, H. M. Weng, B. B. Fu, X. P. Wang, H. Miao, J. Ma, P. Richard, X. C. Huang, L. X. Zhao, G. F. Chen, Z. Fang, X. Dai, T. Qian, and H. Ding, "Experimental discovery of Weyl semimetal TaAs," *Phys. Rev. X* **5**, 031013 (2015).
 - [12] B. Q. Lv, N. Xu, H. M. Weng, J. Z. Ma, P. Richard, X. C. Huang, L. X. Zhao, G. F. Chen, C. E. Matt, F. Bisti, V. N. Strocov, J. Mesot, Z. Fang, X. Dai, T. Qian, M. Shi, and H. Ding, "Observation of Weyl nodes in TaAs," *Nat. Phys.* **11**, 724 (2015).
 - [13] S. Y. Xu, N. Alidoust, I. Belopolski, Z. Yuan, G. Bian, T. R. Chang, H. Zheng, V. N. Strocov, D. S. Sanchez, G. Chang, C. Zhang, D. Mou, Y. Wu, L. Huang, C. C. Lee, S. M. Huang, B. Wang, A. Bansil, H. T. Jeng, T. Neupert, A. Kaminski, H. Lin, S. Jia, and M. Zahid Hasan, "Discovery of a Weyl fermion state with Fermi arcs in niobium arsenide," *Nat. Phys.* **11**, 294 (2015).
 - [14] N. Xu, H. M. Weng, B. Q. Lv, C. E. Matt, J. Park, F. Bisti, V. N. Strocov, D. Gawryluk, E. Pomjakushina, K. Conder, N. C. Plumb, M. Radovic, G. Autes, O. V. Yazyev, Z. Fang, X. Dai, T. Qian, J. Mesot, H. Ding, and M. Shi, "Observation of Weyl nodes and Fermi arcs in tantalum phosphide," *Nat. Commun.* **7** (2016).
 - [15] J. Ruan, S.-K. Jian, H. Yao, H. Zhang, S.-C. Zhang, and D. Xing, "Symmetry-protected ideal Weyl semimetal in HgTe-class materials," *Nat. Commun.* **7**, 11136 (2016).
 - [16] J. Ruan, S.-K. Jian, D. Zhang, H. Yao, H. Zhang, S.-C. Zhang, and D. Xing, "Ideal Weyl semimetals in the chalcopyrites CuTlSe_2 , AgTlTe_2 , AuTlTe_2 , and ZnPbAs_2 ," *Phys. Rev. Lett.* **116**, 226801 (2016).
 - [17] H. B. Nielsen and M. Ninomiya, "The Adler-Bell-Jackiw anomaly and Weyl fermions in a crystal," *Phys. Lett. B* **130**, 389 (1983).
 - [18] G. Xu, H. M. Weng, Z. J. Wang, X. Dai, and Z. Fang, "Chern semimetal and the quantized anomalous Hall effect in HgCr_2Se_4 ," *Phys. Rev. Lett.* **107**, 186806 (2011).
 - [19] K. Y. Yang, Y. M. Lu, and Y. Ran, "Quantum Hall effects in a Weyl semimetal: Possible application in pyrochlore iridates," *Phys. Rev. B* **84**, 075129 (2011).
 - [20] A. A. Zyuzin and A. A. Burkov, "Topological response in Weyl semimetals and the chiral anomaly," *Phys. Rev. B* **86**, 115133 (2012).
 - [21] P. Hosur, S. A. Parameswaran, and A. Vishwanath, "Charge transport in Weyl semimetals," *Phys. Rev. Lett.* **108**, 046602 (2012).
 - [22] D. T. Son and B. Z. Spivak, "Chiral anomaly and classical negative magnetoresistance of Weyl metals," *Phys. Rev. B* **88**, 104412 (2013).
 - [23] M. M. Vazifeh and M. Franz, "Electromagnetic response of Weyl semimetals," *Phys. Rev. Lett.* **111**, 027201 (2013).
 - [24] A. A. Burkov, "Anomalous Hall effect in Weyl metals," *Phys. Rev. Lett.* **113**, 187202 (2014).
 - [25] A. C. Potter, I. Kimchi, and A. Vishwanath, "Quantum oscillations from surface Fermi arcs in Weyl and Dirac semimetals," *Nat. Commun.* **5**, 5161 (2014).
 - [26] A. A. Burkov, "Chiral anomaly and diffusive magnetotransport in Weyl metals," *Phys. Rev. Lett.* **113**, 247203 (2014).
 - [27] S. A. Parameswaran, T. Grover, D. A. Abanin, D. A. Pesin, and A. Vishwanath, "Probing the chiral anomaly with nonlocal transport in three-dimensional topological semimetals," *Phys. Rev. X* **4**, 031035 (2014).
 - [28] H.-Z. Lu, S.-B. Zhang, and S.-Q. Shen, "High-field mag-

- netoconductivity of topological semimetals with short-range potential,” *Phys. Rev. B* **92**, 045203 (2015).
- [29] K. Landsteiner, “Anomalous transport of Weyl fermions in Weyl semimetals,” *Phys. Rev. B* **89**, 075124 (2014).
- [30] J. Zhou, H. R. Chang, and D. Xiao, “Plasmon mode as a detection of the chiral anomaly in Weyl semimetals,” *Phys. Rev. B* **91**, 035114 (2015).
- [31] S.-B. Zhang, H.-Z. Lu, and S.-Q. Shen, “Linear magnetoconductivity in an intrinsic topological Weyl semimetal,” *New J. Phys.* **18**, 053039 (2016).
- [32] C. Zhang, S. Y. Xu, I. Belopolski, Z. Yuan, Z. Lin, B. Tong, N. Alidoust, C. C. Lee, S. M. Huang, T. R. Chang, H. T. Jeng, H. Lin, M. Neupane, D. S. Sanchez, H. Zheng, G. Bian, J. Wang, C. Zhang, H.-Z. Lu, S.-Q. Shen, T. Neupert, M. Zahid Hasan, and S. Jia, “Signatures of the Adler-Bell-Jackiw chiral anomaly in a Weyl fermion semimetal,” *Nat. Commun.* **7**, 10735 (2016).
- [33] Q. Li, D. E. Kharzeev, C. Zhang, Y. Huang, I. Pletikosic, A. V. Fedorov, R. D. Zhong, J. A. Schneeloch, G. D. Gu, and T. Valla, “Chiral magnetic effect in ZrTe_5 ,” *Nat. Phys.* **12**, 550 (2016).
- [34] H. B. Nielsen and M. Ninomiya, “A no-go theorem for regularizing chiral fermions,” *Phys. Lett. B* **105**, 219 (1981).
- [35] S. A. Yang, H. Pan, and F. Zhang, “Chirality-dependent Hall effect in Weyl semimetals,” *Phys. Rev. Lett.* **115**, 156603 (2015).
- [36] Q.-D. Jiang, H. Jiang, H. Liu, Q.-F. Sun, and X. C. Xie, “Topological Imbert-Fedorov shift in Weyl semimetals,” *Phys. Rev. Lett.* **115**, 156602 (2015).
- [37] C.-K. Chan, P. A. Lee, K. S. Burch, J. H. Han, and Y. Ran, “When Chiral Photons Meet Chiral Fermions: Photoinduced Anomalous Hall Effects in Weyl Semimetals,” *Phys. Rev. Lett.* **116**, 026805 (2016).
- [38] J. J. A. Baselmans, A. F. Morpurgo, B. J. van Wees, and T. M. Klapwijk, “Reversing the direction of the supercurrent in a controllable Josephson junction,” *Nature* **397**, 43 (1999).
- [39] A. A. Golubov, M. Yu. Kupriyanov, and E. Il’ichev, “The current-phase relation in Josephson junctions,” *Rev. Mod. Phys.* **76**, 411 (2004).
- [40] M. H. Devoret and R. J. Schoelkopf, “Superconducting circuits for quantum information: An outlook,” *Science* **339**, 1169–1174 (2013).
- [41] Jay M Gambetta, Jerry M Chow, and Matthias Steffen, “Building logical qubits in a superconducting quantum computing system,” *npj Quantum Information* **3**, 2 (2017).
- [42] T. Meng and L. Balents, “Weyl superconductors,” *Phys. Rev. B* **86**, 054504 (2012).
- [43] S.-B. Zhang, F. Dolcini, D. Breunig, and B. Trauzettel, “Appearance of the universal value e^2/h of the zero-bias conductance in a Weyl semimetal-superconductor junction,” *Phys. Rev. B* **97**, 041116 (2018).
- [44] W. Yu, W. Pan, D. L. Medlin, M. A. Rodriguez, S. R. Lee, Z. Q. Bao, and F. Zhang, “ π and 4π Josephson effects mediated by a Dirac semimetal,” *Phys. Rev. Lett.* **120**, 177704 (2018).
- [45] C.-Z. Li, C. Li, L. X. Wang, S. Wang, Z. M. Liao, A. Brinkman, and D. P. Yu, “Bulk and surface states carried supercurrent in ballistic Nb-Dirac semimetal Cd_3As_2 nanowire-Nb junctions,” *Phys. Rev. B* **97**, 115446 (2018).
- [46] C. Li, J. C. de Boer, B. de Ronde, S. V. Ramankutty, E. van Heumen, Y. Huang, A. de Visser, A. A. Golubov, M. S. Golden, and A. Brinkman, “ 4π periodic Andreev bound states in a Dirac semimetal,” *Nat. Mater.* **17**, 875 (2018).
- [47] Y. Kim, M. J. Park, and M. J. Gilbert, “Probing unconventional superconductivity in inversion-symmetric doped Weyl semimetal,” *Phys. Rev. B* **93**, 214511 (2016).
- [48] U. Khanna, D. K. Mukherjee, A. Kundu, and S. Rao, “Chiral nodes and oscillations in the Josephson current in Weyl semimetals,” *Phys. Rev. B* **93**, 121409 (2016).
- [49] K. A. Madsen, E. J. Bergholtz, and P. W. Brouwer, “Josephson effect in a Weyl SNS junction,” *Phys. Rev. B* **95**, 064511 (2017).
- [50] N. Bovenzi, M. Breitzkreiz, P. Baireuther, T. E. O’Brien, J. Tworzydło, I. Adagideli, and C. W. J. Beenakker, “Chirality blockade of Andreev reflection in a magnetic Weyl semimetal,” *Phys. Rev. B* **96**, 035437 (2017).
- [51] A. Chen, D. I. Pikulin, and M. Franz, “Josephson current signatures of Majorana flat bands on the surface of time-reversal-invariant Weyl and Dirac semimetals,” *Phys. Rev. B* **95**, 174505 (2017).
- [52] G. Y. Cho, J. H. Bardarson, Y.-M. Lu, and J. E. Moore, “Superconductivity of doped Weyl semimetals: Finite-momentum pairing and electronic analog of the $^3\text{He-A}$ phase,” *Phys. Rev. B* **86**, 214514 (2012).
- [53] S. Kourtis, J. Li, Z. Wang, A. Yazdani, and B. A. Bernevig, “Universal signatures of Fermi arcs in quasiparticle interference on the surface of Weyl semimetals,” *Phys. Rev. B* **93**, 041109 (2016).
- [54] See Supplemental Material [url] for detailed calculations, which includes Refs. [55–62].
- [55] F. Crepin and B. Trauzettel, “Parity Measurement in Topological Josephson Junctions,” *Phys. Rev. Lett.* **112**, 077002 (2014).
- [56] C. W. J. Beenakker, “Universal limit of critical-current fluctuations in mesoscopic Josephson junctions,” *Phys. Rev. Lett.* **67**, 3836 (1991).
- [57] P. F. Bagwell, “Suppression of the Josephson current through a narrow, mesoscopic, semiconductor channel by a single impurity,” *Phys. Rev. B* **46**, 12573 (1992).
- [58] F. Crépin and B. Trauzettel, “Flux sensitivity of quantum spin Hall rings,” *Physica E* **75**, 379 (2016).
- [59] D. Sticlet, B. Dóra, and J. Cayssol, “Persistent currents in Dirac fermion rings,” *Phys. Rev. B* **88**, 205401 (2013).
- [60] N. Manton, “The Schwinger model and its axial anomaly,” *Ann. Phys.* **159**, 220 (1985).
- [61] M. I. Katsnelson, K. S. Novoselov, and A. K. Geim, “Chiral tunnelling and the Klein paradox in graphene,” *Nat. Phys.* **2**, 620 (2006).
- [62] G. E. Blonder, M. Tinkham, and T. M. Klapwijk, “Transition from metallic to tunneling regimes in superconducting microconstrictions: Excess current, charge imbalance, and supercurrent conversion,” *Phys. Rev. B* **25**, 4515 (1982).
- [63] We consider the case where the Zeeman effect of a magnetic field is significant. However, the Zeeman energy is still small compared to the energy scale for the separation of Weyl nodes. For simplicity, we restrict ourselves to the case without the orbital effect, i.e., the formation of Landau levels. This should be justified for large chemical potentials and small magnetic fields since the system is far from the quantum Hall regime.
- [64] The k_0 and β dependences are moved into the wave function by a unitary transformation.
- [65] P. W. Brouwer and C. W. J. Beenakker, “Anomalous

- temperature dependence of the supercurrent through a chaotic Josephson junction,” *Chaos Soliton. Fract.* **8**, 1249 (1997).
- [66] F. Dolcini and F. Giazotto, “Switching the sign of Josephson current through Aharonov-Bohm interferometry,” *Phys. Rev. B* **75**, 140511 (2007).
- [67] C. W. J. Beenakker, D. I. Pikulin, T. Hyart, H. Schomerus, and J. P. Dahlhaus, “Fermion-parity anomaly of the critical supercurrent in the Quantum spin-Hall effect,” *Phys. Rev. Lett.* **110**, 017003 (2013).
- [68] I. Sochnikov, L. Maier, C. A. Watson, J. R. Kirtley, C. Gould, G. Tkachov, E. M. Hankiewicz, C. Brüne, H. Buhmann, L. W. Molenkamp, and K. A. Moler, “Non-sinusoidal current-phase relationship in Josephson junctions from the 3D topological insulator HgTe,” *Phys. Rev. Lett.* **114**, 066801 (2015).
- [69] G. Tkachov, P. Burset, B. Trauzettel, and E. M. Hankiewicz, “Quantum interference of edge supercurrents in a two-dimensional topological insulator,” *Phys. Rev. B* **92**, 045408 (2015).
- [70] F. Dolcini, M. Houzet, and J. S. Meyer, “Topological Josephson ϕ_0 junctions,” *Phys. Rev. B* **92**, 035428 (2015).
- [71] I. V. Krive, L. Y. Gorelik, R. I. Shekhter, and M. Jonson, “Chiral symmetry breaking and the Josephson current in a ballistic superconductor-quantum wire-superconductor junction,” *Low Temp. Phys.* **30**, 398 (2004).
- [72] J. Bardeen, and J. L. Johnson, “Josephson current flow in pure superconducting-normal-superconducting junctions,” *Phys. Rev. B* **5**, 72 (1972).
- [73] D. L. Maslov, M. Stone, P. M. Goldbart, and D. Loss, “Josephson current and proximity effect in Luttinger liquids,” *Phys. Rev. B* **53**, 1548 (1996).
- [74] A. A. Burkov, “Mirror Anomaly in Dirac Semimetals,” *Phys. Rev. Lett.* **120**, 016603 (2018).
- [75] M. Tinkham, *Introduction to superconductivity* (Courier Corporation, 1996).
- [76] O. Madelung, *Semiconductors: Data Handbook, 3rd ed.* (Springer-Verlag: New York, 2004).

Supplemental Material

Appendix S1: Effective Zeeman term

Performing the unitary transformation $c_{\uparrow(\downarrow)}^{(\sigma)} = (c_{\sigma,\uparrow} \pm c_{\sigma,\downarrow})/\sqrt{2}$, $\sigma \in \{A, B\}$, the Zeeman interaction transforms into

$$\tilde{H}_Z = \begin{pmatrix} h_x & h_z + ih_y & 0 & 0 \\ h_z - ih_y & -h_x & 0 & 0 \\ 0 & 0 & h_x & h_z + ih_y \\ 0 & 0 & h_z - ih_y & -h_x \end{pmatrix} \quad (\text{S1.1})$$

in the basis $(c_{\uparrow}^{(A)}, c_{\downarrow}^{(A)}, c_{\uparrow}^{(B)}, c_{\downarrow}^{(B)})$. The Zeeman field couples spins within the same orbital. The x -component h_x is diagonal, whereas the y - and z -components h_y , h_z are off-diagonal in this basis. One can observe that h_y and h_z couple electrons from different Weyl nodes, i.e., Weyl nodes 1 and 3 to Weyl nodes 2 and 4, whereas h_x couples electrons not only from different Weyl nodes, i.e., Weyl node 1 to Weyl node 3 and Weyl node 2 to Weyl node 4, but also acts within each Weyl node. At low energies, the basis wave functions $\Psi_{\gamma}(\mathbf{r}) = (\psi_{\gamma,\uparrow}(\mathbf{r}), \psi_{\gamma,\downarrow}(\mathbf{r}))$, $\gamma \in \{1, 2, 3, 4\}$, for the Weyl nodes can be found as

$$\begin{aligned} \Psi_{\gamma}(\mathbf{r}) &= e^{i(\mathbf{k}+\mathbf{Q}_{\gamma})\cdot\mathbf{r}}(c_{\uparrow}^{(B)}, c_{\downarrow}^{(A)}), \quad \gamma = 1, 3, \\ \Psi_{\gamma}(\mathbf{r}) &= e^{i(\mathbf{k}+\mathbf{Q}_{\gamma})\cdot\mathbf{r}}(c_{\uparrow}^{(A)}, c_{\downarrow}^{(B)}), \quad \gamma = 2, 4, \end{aligned} \quad (\text{S1.2})$$

where \mathbf{Q}_{γ} is the position of the Weyl node labeled by γ in momentum space. The full spinor basis containing 8 components can be written as

$$\Psi(\mathbf{r}) = (\Psi_1(\mathbf{r}), \Psi_2(\mathbf{r}), \Psi_3(\mathbf{r}), \Psi_4(\mathbf{r})). \quad (\text{S1.3})$$

The projection of the Zeeman interaction (S1.1) onto the spinor (S1.3) results in

$$H_{ij}^Z = \frac{1}{\Omega} \int d\mathbf{r} \psi_i^*(\mathbf{r}) \tilde{H}_Z \psi_j(\mathbf{r}), \quad (\text{S1.4})$$

where ψ_i is the i -th component of the spinor (S1.3), $\Omega = L_x L_y L_z$ with $L_{x,y,z}$ the lengths of the system along three principal directions, respectively. For example, $H_{1,1}^Z$, $H_{1,4}^Z$, and $H_{1,5}^Z$ are explicitly given by

$$\begin{aligned} H_{1,1}^Z &= \frac{1}{\Omega} \int d^3\mathbf{r} e^{-i\mathbf{Q}_1\cdot\mathbf{r}} (0, 0, 1, 0) \tilde{H}_Z e^{i\mathbf{Q}_1\cdot\mathbf{r}} (0, 0, 1, 0)^T = h_x, \\ H_{1,4}^Z &= \frac{1}{\Omega} \int d^3\mathbf{r} e^{-i\mathbf{Q}_1\cdot\mathbf{r}} (0, 0, 1, 0) \tilde{H}_Z e^{i\mathbf{Q}_2\cdot\mathbf{r}} (0, 0, 0, 1)^T = (h_z + ih_y) \frac{\sin(\beta L_x)}{\beta L_x} \frac{\sin(k_0 L_z)}{k_0 L_z}, \\ H_{1,5}^Z &= \frac{1}{\Omega} \int d^3\mathbf{r} e^{-i\mathbf{Q}_1\cdot\mathbf{r}} (0, 0, 1, 0) \tilde{H}_Z e^{i\mathbf{Q}_3\cdot\mathbf{r}} (0, 0, 1, 0)^T = h_x \frac{\sin(k_0 L_z)}{k_0 L_z}. \end{aligned} \quad (\text{S1.5})$$

Suppose the lengths $L_{x,z}$ or separations of Weyl nodes k_0 and β are large enough such that $\beta L_x \gg 1$ and $k_0 L_z \gg 1$. Then, inter-Weyl node couplings, such as $H_{1,4}^Z$ and $H_{1,5}^Z$, vanish. Therefore, the projection of the Zeeman interaction becomes diagonal in the Weyl-node space and gives rise to Eq. (3) in the Letter for each Weyl node.

Appendix S2: Josephson currents

In this section, we calculate the scattering matrix in the N region, the reflection matrix at the interfaces, and finally the Josephson currents.

1. Scattering and interface reflection matrices

We take the positive chirality sector for illustration and consider the Hamiltonian given in the main text and below explicitly

$$h_{\text{BdG}}^+ = \begin{pmatrix} h_{\text{BdG}} & \emptyset \\ \emptyset & h_{\text{BdG}} \end{pmatrix}, \quad (\text{S2.1})$$

$$h_{\text{BdG}} = \begin{pmatrix} -i\partial_{\mathbf{r}} \cdot \mathbf{s} + h(\mathbf{r})s_z - \mu(\mathbf{r})s_0 & \Delta_s(\mathbf{r})e^{i\text{sgn}(z)\phi/2}s_0 \\ \Delta_s(\mathbf{r})e^{-i\text{sgn}(z)\phi/2}s_0 & i\partial_{\mathbf{r}} \cdot \mathbf{s} + h(\mathbf{r})s_z + \mu(\mathbf{r})s_0 \end{pmatrix}, \quad (\text{S2.2})$$

where \emptyset is the 4×4 null matrix, $\mu(\mathbf{r})$, $h(\mathbf{r})$, and $\Delta_s(\mathbf{r})$ are spatially dependent quantities, as described in the main text. The Hamiltonian decouples into two identical blocks given by Eq. (S2.2). In this section, we deal with Eq. (S2.2), which is enough for the transport problem. In the N region, the basis functions at a given energy ε can be written as (the factor $e^{ik_x x + ik_y y}$ is omitted for simplicity)

$$\begin{aligned} \varphi_{e+}(z) &= (\cos \alpha_e, e^{i\theta_{\mathbf{k}}} \sin \alpha_e, 0, 0)^T e^{ik_e z}, & \varphi_{e-}(z) &= (e^{-i\theta_{\mathbf{k}}} \sin \alpha_e, \cos \alpha_e, 0, 0)^T e^{ik_e z}, \\ \varphi_{h+}(z) &= (0, 0, \cos \alpha_h, -e^{i\theta_{\mathbf{k}}} \sin \alpha_h)^T e^{ik_h z}, & \varphi_{h-}(z) &= (0, 0, -e^{-i\theta_{\mathbf{k}}} \sin \alpha_h, \cos \alpha_h)^T e^{ik_h z}, \end{aligned} \quad (\text{S2.3})$$

where $\theta_{\mathbf{k}} = \arctan(k_y/k_x)$, $\alpha_{e(h)} = \arctan(k_{\parallel}/k_{e(h)})/2$, $k_{\parallel} = (k_x^2 + k_y^2)^{1/2}$, $k_{e\pm} = -h_x \pm k_e$, $k_{h\pm} = h_x \pm k_h$ and $k_{e(h)} = [(\varepsilon \pm \mu_N)^2 - k_{\parallel}^2]^{1/2}$. T means the transpose of a matrix. In the two S regions, the basis functions are

$$\begin{aligned} \varphi_{qe+}(z) &= (e^{i\beta} \cos \tilde{\alpha}_e, e^{i\beta} e^{i\theta_{\mathbf{k}}} \sin \tilde{\alpha}_e, e^{-i\phi_t} \cos \tilde{\alpha}_e, e^{-i\phi_t} e^{i\theta_{\mathbf{k}}} \sin \tilde{\alpha}_e)^T e^{i\tilde{k}_e z}, \\ \varphi_{qe-}(z) &= (e^{i\beta} e^{-i\theta_{\mathbf{k}}} \sin \tilde{\alpha}_e, e^{i\beta} \cos \tilde{\alpha}_e, e^{-i\phi_t} e^{-i\theta_{\mathbf{k}}} \sin \tilde{\alpha}_e, e^{-i\phi_t} \cos \tilde{\alpha}_e)^T e^{-i\tilde{k}_e z}, \\ \varphi_{qh+}(z) &= (e^{i\phi_t} \sin \tilde{\alpha}_h, e^{i\phi_t} e^{i\theta_{\mathbf{k}}} \cos \tilde{\alpha}_h, e^{i\beta} \sin \tilde{\alpha}_h, e^{i\beta} e^{i\theta_{\mathbf{k}}} \cos \tilde{\alpha}_h)^T e^{-i\tilde{k}_h z}, \\ \varphi_{qh-}(z) &= (e^{i\phi_t} e^{-i\theta_{\mathbf{k}}} \cos \tilde{\alpha}_h, e^{i\phi_t} \sin \tilde{\alpha}_h, e^{i\beta} e^{-i\theta_{\mathbf{k}}} \cos \tilde{\alpha}_h, e^{i\beta} \sin \tilde{\alpha}_h)^T e^{i\tilde{k}_h z}, \end{aligned} \quad (\text{S2.4})$$

where $t \in \{r, l\}$ labels the pairing phases $\phi_l = -\phi/2$ and $\phi_r = \phi/2$ on the left and right hand sides, respectively; $\tilde{\alpha}_{e(h)} = \arctan(k_{\parallel}/\tilde{k}_{e(h)})/2$ and $\tilde{k}_{e(h)} = [(\mu_S \pm \Omega)^2 - k_{\parallel}^2]^{1/2}$. For subgap energies $\varepsilon \leq \Delta$, $\beta = \arccos(\varepsilon/\Delta)$, and $\Omega = i(\Delta^2 - \varepsilon^2)^{1/2}$, while for supragap energies $\varepsilon > \Delta$, $\beta = -i\text{arccosh}(\varepsilon/\Delta)$, and $\Omega = \text{sgn}(\varepsilon)(\varepsilon^2 - \Delta^2)^{1/2}$. Therefore, the wave function can be expanded in terms of these basis functions as

$$\Psi(z) = \begin{cases} N_{e+}\varphi_{e+}(z) + N_{e-}\varphi_{e-}(z) + N_{h+}\varphi_{h+}(z) + N_{h-}\varphi_{h-}(z), & |z| < L/2, \\ S_{e+}\varphi_{qe+}(z) + S_{e-}\varphi_{qe-}(z) + S_{h+}\varphi_{qh+}(z) + S_{h-}\varphi_{qh-}(z), & |z| > L/2, \end{cases} \quad (\text{S2.5})$$

where superposition coefficients $N_{e(h)\pm}$ and $S_{e(h)\pm}$ are determined by the boundary conditions.

The reflection matrix is then determined by matching the wave function in Eq. (S2.5) at the interfaces at $z = \pm L/2$ and found explicitly as

$$\mathcal{R}_A^+ = \begin{pmatrix} R_{ee}e^{-i\theta_{\mathbf{k}}} & R_{eh}e^{-i\phi/2} & 0 & 0 \\ R_{he}e^{i\phi/2} & R_{hh}e^{i\theta_{\mathbf{k}}} & 0 & 0 \\ 0 & 0 & R_{ee}e^{i\theta_{\mathbf{k}}} & R_{eh}e^{i\phi/2} \\ 0 & 0 & R_{he}e^{-i\phi/2} & R_{hh}e^{-i\theta_{\mathbf{k}}} \end{pmatrix}, \quad (\text{S2.6})$$

where

$$\begin{aligned} R_{ee} &= -[e^{i\beta} \sin(\alpha_e - \tilde{\alpha}_e) \sin(\alpha_h + \tilde{\alpha}_h) - e^{-i\beta} \sin(\alpha_h + \tilde{\alpha}_e) \sin(\alpha_e - \tilde{\alpha}_h)]/\mathcal{Z}, \\ R_{eh} &= -\cos(2\alpha_h) \sin(\tilde{\alpha}_e - \tilde{\alpha}_h)/\mathcal{Z}, & R_{he} &= -\cos(2\alpha_e) \sin(\tilde{\alpha}_e - \tilde{\alpha}_h)/\mathcal{Z}, \\ R_{hh} &= [e^{i\beta} \cos(\alpha_e + \tilde{\alpha}_e) \cos(\alpha_h - \tilde{\alpha}_h) - e^{-i\beta} \cos(\alpha_e + \tilde{\alpha}_h) \cos(\alpha_h - \tilde{\alpha}_e)]/\mathcal{Z}, \end{aligned} \quad (\text{S2.7})$$

with $\mathcal{Z} = e^{i\beta} \cos(\alpha_e + \tilde{\alpha}_e) \sin(\alpha_h + \tilde{\alpha}_h) - e^{-i\beta} \cos(\alpha_e + \tilde{\alpha}_h) \sin(\alpha_h + \tilde{\alpha}_e)$ [?]. The reflection matrix is block-diagonal with two blocks describing the reflection property of the two interfaces, respectively. Assume that the N region is clean enough such that no scattering occurs between different modes. The scattering matrix is then given by the dynamic phases accumulated as the particles and holes propagate along the N region:

$$\mathcal{S}_N^+ = \begin{pmatrix} 0 & 0 & e^{-ik_e L} & 0 \\ 0 & 0 & 0 & e^{-ik_h L} \\ e^{ik_e L} & 0 & 0 & 0 \\ 0 & e^{ik_h L} & 0 & 0 \end{pmatrix}. \quad (\text{S2.8})$$

The Zeeman field h_x does not alter the basis states but only enters the wave vectors $k_{e\pm}$ and $k_{h\pm}$ which are canceled out on matching the wave function. Therefore, h_x does not affect the reflection \mathcal{R}_A^+ but scattering matrix \mathcal{S}_N^+ ,

2. Josephson current

We apply the method described in Refs. [? ? ?] to calculate the Josephson current densities

$$J_s^\pm(\phi) = -\frac{16ek_BT}{\hbar} \sum_{\mathbf{k}_\parallel} \sum_{n=0}^{\infty} \frac{d}{d\phi} \ln D_\pm(\mathbf{k}_\parallel, \phi; i\omega_n), \quad (\text{S2.9})$$

where the sums run over all transverse momenta \mathbf{k}_\parallel and fermionic Matsubara frequencies $\omega_n = (2n+1)\pi k_BT$, $-e$ is the electron charge, T the temperature, k_B the Boltzmann constant and $D_\pm = \det(1 - \mathcal{R}_A^\pm \mathcal{S}_N^\pm)$. The index $+$ ($-$) denotes positive(negative) chirality. This method takes into account both contributions from discrete Andreev bound states and the continuum spectrum. The condition $D_\pm(\mathbf{k}_\parallel, \phi; \varepsilon) = \mathbf{0}$ determines the energy spectrum of Andreev bound states with energy within the superconducting gap.

With Eqs. (S2.6) and (S2.8), D_+ is obtained as

$$D_+ = 1 - R_{ee}^2 e^{2ik_e L} - R_{hh}^2 e^{2ik_h L} + (R_{ee}R_{hh} - R_{eh}R_{he})^2 e^{2i(k_e+k_h)L} - 2R_{eh}R_{he} \cos \phi' e^{i(k_e+k_h)L}. \quad (\text{S2.10})$$

The phase dependence in D_+ comes from the finite Andreev reflection at the interfaces. The Zeeman field h_x leads directly to a shift in the phase difference $\phi' = \phi + \phi_0$ with $\phi_0 = 2h_x L$. For $\mu_N = \mu_S \gg \Delta$, $R_{ee} \approx R_{hh} \approx 0$ and $R_{eh} \approx R_{he} \approx e^{-i\beta}$.

3. Josephson current in the long junction and zero temperature limit

In the long junction and zero temperature limit, only low-energy Andreev bound states with energy $|\epsilon| \ll \Delta$ are relevant for the Josephson current [?]. For simplicity, we put $\Delta \rightarrow \infty$ so that the low-energy states are well localized in the N region. Andreev bound states are determined by the condition $D_\pm = 0$. But here, we can make use of the long junction assumption and find the Andreev bound states by using the method of Ref. [?]. For a given transverse momentum \mathbf{k}_\parallel , there are two Fermi points $\pm k_F$ satisfying $(k_F^2 + k_\parallel^2)^{1/2} = \mu_N$ (we assume $\mu_N > 0$ without loss of generality). If we take $k_z = \pm k_F + q_z$ with q_z small, then the low-energy excitations measured from μ_N are described by a helical model

$$H_1 = v_F q_z \sigma'_z, \quad (\text{S2.11})$$

where $v_F = (\mu_N^2 - k_\parallel^2)^{1/2}/\mu_N$ is the effective Fermi velocity and the Pauli matrix σ'_z acts on the two chiral bands. For the positive and negative chirality sectors, the allowed values of q_z that satisfy the boundary conditions [55] at $L = \pm L/2$ are found as

$$q_n^\pm = \frac{\pi}{L} \left(n + \frac{1}{2} + \frac{\phi \pm \phi_0}{2\pi} \right), \quad n \in \mathbb{Z}, \quad (\text{S2.12})$$

respectively. Both the phase difference and Zeeman field have been taken into account. Therefore, the energies of Andreev bound states are

$$\epsilon_{n,\eta}^\pm = \eta \frac{\pi v_F}{L} \left(n + \frac{1}{2} + \frac{\phi \pm \phi_0}{2\pi} \right), \quad \eta \in \{-1, 1\}. \quad (\text{S2.13})$$

Note that for $k_\parallel = 0$, ϵ_n can also be found easily by solving $D_\pm = 0$ with $\epsilon/\Delta \rightarrow 0$. The result is in agreement with Eq. (S2.13). These energy levels are linear in $\phi \pm \phi_0$ and cross at $\phi \pm \phi_0 = \pi$ (and other quantized values $\phi \pm \phi_0 = (2n+1)\pi$ with $n \in \mathbb{Z}$). The level crossings at $\phi \pm \phi_0 = (2n+1)\pi$ are protected by a pseudo time-reversal symmetry (with the operator $i\mathcal{K}\sigma'_y$, \mathcal{K} is the complex conjugation).

The Josephson currents of each chirality can be related to the eigenenergies by [56, 57]

$$J_s^\pm = \sum_{\mathbf{k}_\parallel} j_s^\pm, \quad j_s^\pm = \frac{e}{\hbar} \frac{\partial F_\pm(\phi)}{\partial \phi}, \quad F_\pm(\phi) = 2 \sum_n \epsilon_{n,\eta}^\pm f_F(\epsilon_{n,\eta}^\pm), \quad (\text{S2.14})$$

where F_{\pm} is the free energy and $f_F(E)$ is the Fermi distribution function. At zero temperature, $f_F(E) = \Theta(-E)$. Due to the linearized spectrum, there are infinitely many negative energy states forming the Dirac sea. Nevertheless, $J_s^{\pm}(\phi)$ can be calculated by the method of Bosonization [58] or ultraviolet regularization [59, 60] since the energy states deep in the Dirac sea have exponentially small contribution to the physical properties of the system. For $-\pi < \phi \pm \phi_0 < 3\pi$, j_s^{\pm} is found as

$$j_s^{\pm} = \frac{2\pi v_F}{L} \left[\frac{\phi \pm \phi_0}{\pi} - \text{sgn}(\phi \pm \phi_0 - \pi) - 1 \right]. \quad (\text{S2.15})$$

For each \mathbf{k}_{\parallel} , the supercurrent has a piecewise phase-dependence with a discontinuous jump at $\phi \pm \phi_0 = \pi$. Summing over \mathbf{k}_{\parallel} and taking the difference of J_s^{\pm} , we obtain the chirality Josephson current. At $\phi = \pi$, the chirality Josephson current J_s^{chi} for small $h_x L$ is given by

$$J_s^{\text{chi}} = \frac{2\mu_N^2}{3L} \left[\frac{2h_x L}{\pi} - \text{sgn}(h_x) \right], \quad |h_x L| < \pi. \quad (\text{S2.16})$$

It shows a discontinuous jump at $h_x = 0$ (see Fig. S5).

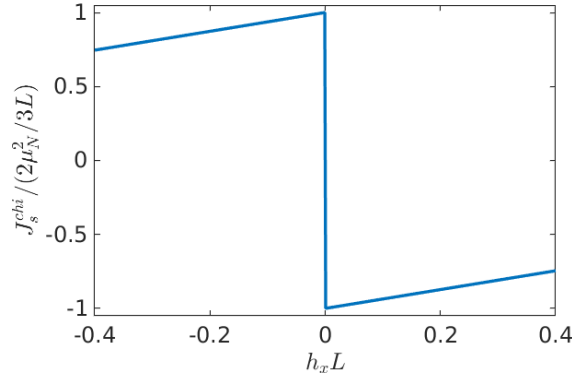


Figure S5. Chirality Josephson current J_s^{chi} at $\phi = \pi$ and $T = 0$ as a function of $h_x L$ in a long Josephson junction $L \gg 1/\Delta$.

The discontinuity in Eq. (S2.16) is robust against a non-magnetic and perturbative impurity barrier modeled by a scalar potential $U(\mathbf{r}) = \delta U [\Theta(z - z_1) - \Theta(z - z_2)]$ with $-L/2 \leq z_1 < z_2 \leq L/2$. For simplicity, we assume a uniform barrier potential $U(\mathbf{r})$ in x and y directions. Then, the transverse momentum \mathbf{k}_{\parallel} is preserved. This potential may account for an interface barrier or smooth (particularly in x and y directions) disorder in the N region. If δU is small enough such that the linearized model remains valid, then, the scalar potential only generates phase shifts for the two chiral particles without coupling them. By imposing the boundary conditions, the energies of Andreev bound states are found as

$$\epsilon_{n,\eta}^{\pm} = \eta \frac{\pi v_F}{L} \left(n + \frac{1}{2} + \frac{\phi \pm \phi_0}{2\pi} \right) + U_0, \quad \eta \in \{-1, 1\}, \quad (\text{S2.17})$$

where $U_0 = (z_2 - z_1)\delta U/L$. The only effect of the impurity barrier is to shift the spectrum by a global constant U_0 which does not depend on the phase difference. The energy crossings at $\phi \pm \phi_0 = \pi$ of the clean spectrum in Eq. (S2.13) are thus preserved since the scalar potential does not break the underlying pseudo time-reversal symmetry. This behavior is a manifestation of the absence of backscattering or Klein tunneling [61] in a helical liquid. Plugging Eq. (S2.17) into Eq. (S2.14), we arrive at exactly the same formulas as Eqs. (S2.15) and (S2.16). Note that, for magnetic or strong impurities [57], backscattering is no longer prohibited. It opens gaps between the energy levels of the two chiral particles. Then, the discontinuity in Eq. (S2.16) will be smoothed out.

Appendix S3: Normal-state resistance of the junction

In this section, we apply the scattering matrix formalism [62] to calculate the normal-state resistance of the junction. The wave function of a scattering state in which an electron is incident on the left-hand side and moves to the right

is given by

$$\Psi(z) = \begin{cases} \bar{\varphi}_{\leftarrow}(z) + r_0 \bar{\varphi}_{\leftarrow}(z), & z < -L/2, \\ \alpha_0 \varphi_{\leftarrow}(z) + \beta_0 \varphi_{\leftarrow}(z), & |z| < L/2, \\ t_0 \bar{\varphi}_{\leftarrow}(z), & z > L/2. \end{cases} \quad (\text{S3.1})$$

Consider the scattering state at the Fermi level. Then, the basis functions are given by

$$\begin{aligned} \varphi_{\leftarrow}(z) &= (\cos(\alpha/2), \sin(\alpha/2))^T e^{ik_e z}, & \varphi_{\leftarrow}(z) &= (\sin(\alpha/2), \cos(\alpha/2))^T e^{-ik_e z}, \\ \bar{\varphi}_{\leftarrow}(z) &= (\cos(\bar{\alpha}/2), \sin(\bar{\alpha}/2))^T e^{i\bar{k}_e z}, & \bar{\varphi}_{\leftarrow}(z) &= (\sin(\bar{\alpha}/2), \cos(\bar{\alpha}/2))^T e^{-i\bar{k}_e z}, \end{aligned} \quad (\text{S3.2})$$

where the angles α and $\bar{\alpha}$ are defined by $\sin \alpha = k_{\parallel}/\mu_N$, $\cos \alpha = k_e/\mu_N$, $\sin \bar{\alpha} = k_{\parallel}/\mu_S$ and $\cos \bar{\alpha} = \bar{k}_e/\mu_S$, respectively. Note that the scattering state exists only when $\bar{k}_e = (\mu_S^2 - k_{\parallel}^2)^{1/2}$ is real. The coefficients α_0 , β_0 , t_0 and r_0 are determined by requiring the continuity of $\Psi(z)$ at the interfaces at $z = \pm L/2$. The transmission probability $T_0 \equiv |t_0|^2$ of current density across the junction can be found as

$$T_0 = \left| \frac{\cos \alpha \cos \bar{\alpha}}{\cos \alpha \cos \bar{\alpha} \cos(k_e L) + i(\sin \alpha \sin \bar{\alpha} - 1) \sin(k_e L)} \right|^2. \quad (\text{S3.3})$$

This implies that T_0 is an oscillatory function of the junction length L for $\mu_N > \mu_S$. For the short junction limit with $L = 0$, a uniform chemical potential $\mu_N = \mu_S$, or normal incidence $k_{\parallel} = 0$, we obtain the perfect transmission $T_0 = 1$.

The resistance of the junction at zero temperature can then be calculated by the Landauer formula

$$R_n^{-1} = \frac{4e^2}{h} \sum_{\mathbf{k}_{\parallel}} T_0(\mathbf{k}_{\parallel}), \quad (\text{S3.4})$$

where the factor 4 is due to four Weyl cones in the system. For $\mu_N = \mu_S$ or $L = 0$, $R_n = (h/e^2)(\pi/\mu_S^2)$.

Appendix S4: Symmetry analysis

At low energies, the Hamiltonian for the two Weyl nodes of positive chirality can be written as

$$H_+(\mathbf{r}) = -i\tau_0(\partial_x s_x + \partial_y s_y + \partial_z s_z) - \tau_z(\beta s_x + k_0 s_z)$$

in the basis $\tilde{\Psi}_+ = (e^{-i\mathbf{Q}_1 \cdot \mathbf{r}} \Psi_1, e^{-i\mathbf{Q}_2 \cdot \mathbf{r}} \Psi_2)$. Here, s_i and τ_i ($i = 0, x, y, z$) act in spin and Weyl-node spaces, respectively. For the Weyl nodes of negative chirality, the Hamiltonian reads

$$H_-(\mathbf{r}) = -i\tau_0(\partial_x s_x + \partial_y s_y - \partial_z s_z) - \tau_z(\beta s_x + k_0 s_z)$$

in the basis $\tilde{\Psi}_- = (e^{-i\mathbf{Q}_3 \cdot \mathbf{r}} \Psi_3, e^{-i\mathbf{Q}_4 \cdot \mathbf{r}} \Psi_4)$. According to Eq. (S1.2), the Hamiltonian for opposite chirality share the same basis $\tilde{\Psi}_+ = \tilde{\Psi}_- = (c_{\uparrow}^{(B)}, c_{\downarrow}^{(A)}, c_{\uparrow}^{(A)}, c_{\downarrow}^{(B)})$. In this basis, the time-reversal operator reads $\mathcal{T} = -i\tau_x s_y \mathcal{K}$, where \mathcal{K} denotes the complex conjugation. In addition, there exists an emergent symmetry operation

$$\mathcal{U} = i\tau_y s_y \mathcal{R}_x = e^{i\pi s_y \tau_y R_x/2}, \quad (\text{S4.1})$$

where \mathcal{R}_x is the reflection operator about the yz plane, (i.e., $x \rightarrow -x$). In the absence of magnetic fields, each chirality sector is invariant under time-reversal, i.e., $[H_{\pm}(\mathbf{r}), \mathcal{T}] = 0$. They are connected to each other by the emergent symmetry, i.e., $\mathcal{U}H_+(\mathbf{r})\mathcal{U}^{-1} = H_-(\mathbf{r})$. In the full basis spinor $(\tilde{\Psi}_+, \tilde{\Psi}_-)$, we can define an operator as

$$\mathcal{U}_5 = \begin{pmatrix} \emptyset & \mathcal{U} \\ \mathcal{U} & \emptyset \end{pmatrix}. \quad (\text{S4.2})$$

which commutes with the full Hamiltonian $H = \text{diag}(H_+(\mathbf{r}), H_-(\mathbf{r}))$, i.e., $[H, \mathcal{U}_5] = 0$. This implies that the system has a discrete \mathbb{Z}_2 symmetry which exchanges the two chirality sectors. We thus call \mathcal{U} the \mathbb{Z}_2 (exchange) symmetry.

The BdG Hamiltonians for the two chirality sectors can be written as

$$\mathcal{H}_{\text{BdG}}^{\pm}(\phi) = \begin{pmatrix} H_{\pm}(\mathbf{r}) - \mu(\mathbf{r})\tau_0 s_0 & i\Delta_s(\mathbf{r})e^{i\text{sgn}(z)\phi/2}\tau_x s_y \\ -i\Delta_s(\mathbf{r})e^{-i\text{sgn}(z)\phi/2}\tau_x s_y & -H_{\pm}^*(\mathbf{r}) + \mu(\mathbf{r})\tau_0 s_0 \end{pmatrix} \quad (\text{S4.3})$$

in the Nambu basis $(c_{\uparrow}^{(B)}, c_{\downarrow}^{(A)}, c_{\uparrow}^{(A)}, c_{\downarrow}^{(B)}, c_{\uparrow}^{(B)\dagger}, c_{\downarrow}^{(A)\dagger}, c_{\uparrow}^{(A)\dagger}, c_{\downarrow}^{(B)\dagger})$. Accordingly, the extended operator of \mathcal{U} in this Nambu basis reads $\mathcal{U}_{\text{BdG}} = \text{diag}(\mathcal{U}, -\mathcal{U})$. It relates the BdG Hamiltonians as

$$\mathcal{U}_{\text{BdG}} \mathcal{H}_{\text{BdG}}^+(\phi) \mathcal{U}_{\text{BdG}}^{-1} = \mathcal{H}_{\text{BdG}}^-(\phi). \quad (\text{S4.4})$$

The BdG equation for positive chirality is described by

$$\mathcal{H}_{\text{BdG}}^+(\phi) \psi_n^+ = E_n^+(\phi) \psi_n^+, \quad (\text{S4.5})$$

where ψ_n and E_n are eigenstate and eigenenergy labeled by an index n , respectively. Making use of Eq. (S4.4), Eq. (S4.5) can be transformed to

$$\mathcal{H}_{\text{BdG}}^-(\phi) \mathcal{U}_{\text{BdG}} \psi_n^+ = E_n^+(\phi) \mathcal{U}_{\text{BdG}} \psi_n^+. \quad (\text{S4.6})$$

This indicates that $\mathcal{H}_{\text{BdG}}^{\pm}(\phi)$ have exactly the same eigenenergies. Namely,

$$E_n^-(\phi) = E_n^+(\phi). \quad (\text{S4.7})$$

Using the formula for the Josephson currents of each chirality

$$J_s^{\pm}(\phi) = \frac{e}{\hbar} \frac{\partial F_{\pm}(\phi)}{\partial \phi}, \quad F_{\pm}(\phi) = \sum_n E_n^{\pm} f_F(E_n^{\pm}). \quad (\text{S4.8})$$

With the help of Eq. (S4.7), we find that the Josephson currents for the two chirality sectors have to be equal,

$$J_s^+(\phi) = J_s^-(\phi). \quad (\text{S4.9})$$

The presence of h_x breaks both the symmetries \mathcal{T} and \mathcal{U} simultaneously. However, the system preserves a combined symmetry defined by the product of \mathcal{T} and \mathcal{U} ,

$$\mathcal{S} = \mathcal{T}\mathcal{U} = -i\tau_z \mathcal{R}_x \mathcal{K}, \quad (\text{S4.10})$$

as represented explicitly by

$$\mathcal{S}[H_+(\mathbf{r}) + h(\mathbf{r})\tau_0 s_z] \mathcal{S}^{-1} = H_-(\mathbf{r}) + h(\mathbf{r})\tau_0 s_z. \quad (\text{S4.11})$$

Thus, \mathcal{S} exchanges the two chirality sectors even in the presence of h_x . We call it a magnetic \mathbb{Z}_2 symmetry. In the presence of h_x , the BdG Hamiltonians (S4.3) are modified to

$$\tilde{\mathcal{H}}_{\text{BdG}}^{\pm}(\phi) = \begin{pmatrix} H_{\pm}(\mathbf{r}) + h(\mathbf{r})\tau_0 s_z - \mu(\mathbf{r})\tau_0 s_0 & i\Delta_s(\mathbf{r})e^{i\text{sgn}(z)\phi/2}\tau_x s_y \\ -i\Delta_s(\mathbf{r})e^{-i\text{sgn}(z)\phi/2}\tau_x s_y & -H_{\pm}^*(\mathbf{r}) - h(\mathbf{r})\tau_0 s_z - \mu(\mathbf{r})\tau_0 s_0 \end{pmatrix}. \quad (\text{S4.12})$$

They are related by

$$\mathcal{S}_{\text{BdG}} \mathcal{H}_{\text{BdG}}^+(\phi) \mathcal{S}_{\text{BdG}}^{-1} = \mathcal{H}_{\text{BdG}}^-(\phi), \quad (\text{S4.13})$$

with $\mathcal{S}_{\text{BdG}} = \text{diag}(\mathcal{S}, -\mathcal{S})$ the corresponding extended operator of \mathcal{S} in the Nambu basis. In this case, we do not have the relation in Eq. (S4.6) but still

$$\mathcal{H}_{\text{BdG}}^-(\phi) \mathcal{S}_{\text{BdG}} \psi_n^+ = E_n^+(-\phi) \mathcal{S}_{\text{BdG}} \psi_n^+. \quad (\text{S4.14})$$

Consequently,

$$E_n^-(\phi) \neq E_n^+(\phi), \quad E_n^-(\phi) = E_n^+(-\phi). \quad (\text{S4.15})$$

Therefore, using Eq. (S4.8), we find $J_s^+(\phi) \neq J_s^-(\phi)$, and

$$J_s^+(\phi) = -J_s^+(-\phi). \quad (\text{S4.16})$$

The relation in Eq. (S4.16) holds even in the presence of h_x which breaks time-reversal symmetry.

Appendix S5: Fraunhofer patterns

As shown in Figs. S6, S7 and S8, although the CPR is sensitive to junction lengths, low temperatures, and chemical potentials, the corresponding Fraunhofer patterns are almost the same. For $\tilde{g} \neq 0$, the supercurrents of opposite chirality vary differently as increasing the magnetic field. As a consequence, an anomalous Fraunhofer pattern occurs as the interference of the two different supercurrents. Therefore, the anomalous Fraunhofer pattern is an indication of the finite chirality Josephson currents in the system. At large temperatures, the sinusoidal form of CPR can be observed. Thus, all the minima drop to zero [Fig. S8(b, c)].

Since different choices of $J_s^{\text{tot}}(\phi)$ yield more or less the same Fraunhofer pattern, we can assume the usual sinusoidal CPR for each chirality and obtain a simple formula

$$\frac{I_c(\Phi)}{I_c(0)} = \frac{\Phi_0}{\pi\Phi} \left| \sin\left(\frac{\pi\Phi}{\Phi_0}\right) \cos\left(\frac{\tilde{g}\Phi}{\Phi_0}\right) \right|. \quad (\text{S5.1})$$

Although the true CPR is usually skewed forward, Eq. (S5.1) captures the correct Fraunhofer patterns quite well (Fig. 4 in the Letter). From this analogy, the two frequencies of Φ/Φ_0 can be extracted as $2/(1 \pm \tilde{g}/\pi)$, respectively. $I_c(\Phi)$ vanishes not only at every nonzero integer $\Phi/\Phi_0 \in \{\pm 1, \pm 2, \dots\}$, but also at $\Phi/\Phi_0 = (n + 1/2)\pi/\tilde{g}$, $n \in \mathbb{Z}$. The skewed form in $J_s^\pm(\phi)$, however, removes the zeros of $I_c(\Phi)$ at $\Phi/\Phi_0 = (n + 1/2)\pi/\tilde{g}$ and leaves finite minima there.

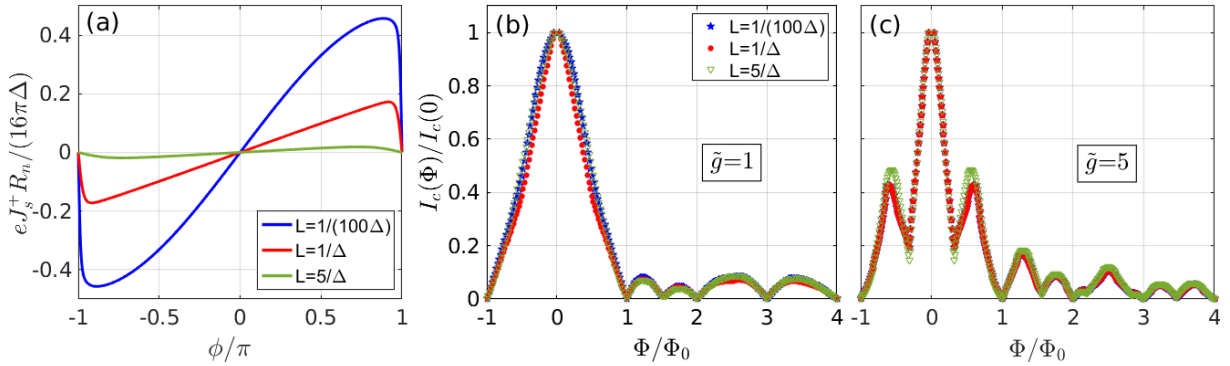


Figure S6. Current-phase relations for positive chirality in the absence of magnetic fields (a) and Fraunhofer patterns for $\tilde{g} = 1$ (b) and 5 (c) in junctions with lengths $L = 1/(100\Delta)$, $1/\Delta$, and $5/\Delta$, respectively. Other parameters are $\mu_S = \mu_N = 100\Delta$ and $k_B T = 0.01\Delta$.

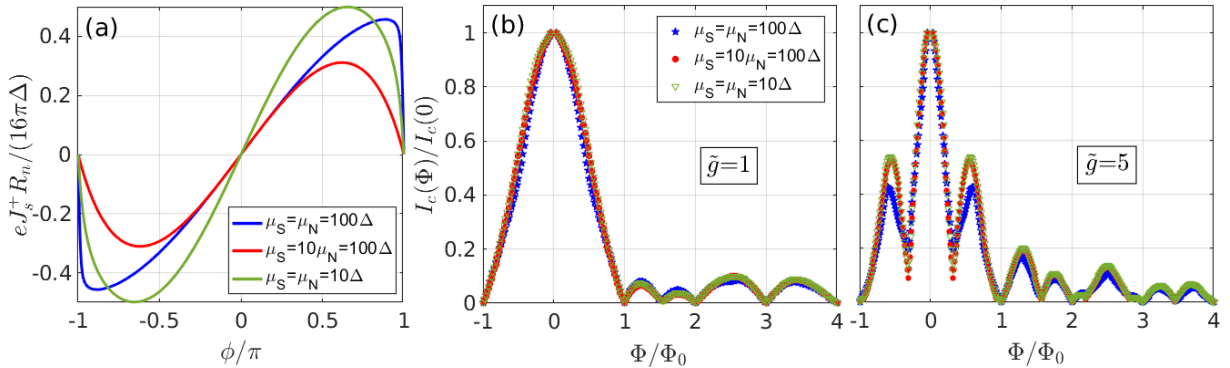


Figure S7. Current-phase relations for positive chirality in the absence of magnetic fields (a) and Fraunhofer patterns for $\tilde{g} = 1$ (b) and 5 (c) in junctions with chemical potentials $\mu_S = \mu_N = 100\Delta$, $\mu_S = 10\mu_N = 100\Delta$, and $\mu_S = \mu_N = 10\Delta$, respectively. Other parameters are $L = 1/(100\Delta)$ and $k_B T = 0.01\Delta$.

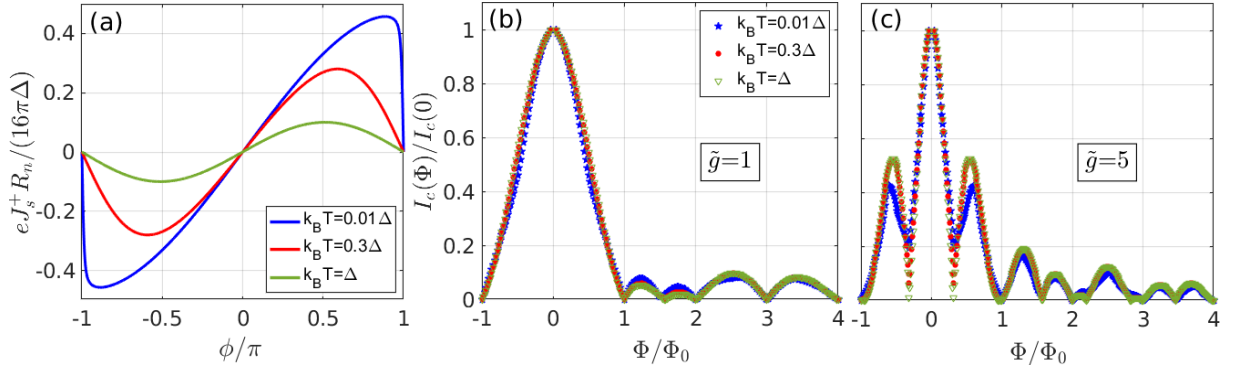


Figure S8. Current-phase relations for positive chirality in the absence of magnetic fields (a) and Fraunhofer patterns for $\tilde{g} = 1$ (b) and 5 (c) at temperature $k_B T = 0.01\Delta$, 0.3Δ , and Δ , respectively. Other parameters are $\mu_S = \mu_N = 100\Delta$ and $L = 1/(100\Delta)$.